Vortex formation in a strongly coupled dusty plasma flow past an obstacle

9 authors, including:

Yoshiko Bailung
Institute of Advanced Study in Science and Technology
8 PUBLICATIONS   **32** CITATIONS

Bidyut Chutia
Centre of Plasma Physics-Institute for Plasma Research (CPP-IPR)
7 PUBLICATIONS   **24** CITATIONS

Tonuj Deka
Institute of Advanced Study in Science and Technology
8 PUBLICATIONS   **50** CITATIONS

Abhijit Boruah
Institute for Plasma Research
8 PUBLICATIONS   **172** CITATIONS

Some of the authors of this publication are also working on these related projects:

Project   Plasma physics View project

Project   Studies of statics and dynamical structures in dusty plasma View project

Vortex formation in a strongly coupled dusty plasma flow past an obstacle

Yoshiko Bailung, Bidyut Chutia, T. Deka, A. Boruah, Sumita K. Sharma, Sandeep Kumar, Joyanti Chutia, Y. Nakamura, and H. Bailung

View Online   Export Citation   CrossMark

ARTICLES YOU MAY BE INTERESTED IN

Vortex formation in a strongly coupled dusty plasma flow past an obstacle

View Online   Export Citation   CrossMark

Yoshiko Bailung,[1] (iD) Bidyut Chutia,[1] (iD) T. Deka,[1] (iD) A. Boruah,[1] (iD) Sumita K. Sharma,[1] (iD) Sandeep Kumar,[2] (iD)
Joyanti Chutia,[1] (iD) Y. Nakamura,[1] (iD) and H. Bailung[1,a] (iD)

AFFILIATIONS

[1]Dusty Plasma Laboratory, Physical Sciences Division, Institute of Advanced Study in Science and Technology, Paschim Boragaon,
 Garchuk, Guwahati, Assam 781035, India
[2]Institute of Physics, University of Rostock, A-Einstein Str. 23, D-18059 Rostock, Germany

[a]Author to whom correspondence should be addressed: hbailung@yahoo.com

ABSTRACT

A pair of counter-rotating symmetric vortices has been observed in the wake behind a stationary obstacle (dust void) in a flowing dusty plasma. A strongly coupled dusty plasma flow with controllable velocity is generated and directed toward the void in a novel experiment. In the unsteady laminar flow regime, the curl of the fluid flow velocity along the boundary layer of the void generates the vortex pair behind the void. Particle image velocimetry analysis of high speed image data clearly depicts the flow pattern and the vorticities. The shear viscosity of the dusty plasma fluid along with the experimental parameters is considered to obtain the Reynolds number range for the evolution of the vortices. Molecular dynamics simulation is also performed to support the experimental observation.

Published under license by AIP Publishing. https://doi.org/10.1063/5.0022356

I. INTRODUCTION

A dusty plasma is a unique medium consisting of electrons, ions, and neutrals with additional micrometer or submicrometer sized charged particles. Due to the presence of a highly charged and massive component, dusty plasmas are involved in a wide variety of physical and chemical processes. They have been explored as a model system for different dynamical processes (e.g., phase transition, transport phenomena).[1,2] The complex plasmas behave as many-particle interacting systems and provide a unique opportunity to investigate various organized collective effects prevalent in fluids, clusters, crystals, etc., in greater temporal resolution as they appear on a slower timescale.[3,4] Charge particle flow past an obstacle posed by electric or magnetic fields creates complex dynamics and associated effects (shocks, instabilities, vortices and turbulence, etc.). In particular, vortices are considered to be a significant component of turbulent flow. Studies on such dynamics are very much relevant to the astrophysical context.[5] Auroral display is a unique phenomenon associated with solar wind plasma flow past a planet with a magnetic field (e.g., the Earth).

Self-generated vortex flows are observed in many dusty plasma experiments and have been dealt with considerable attention in the last few years. In a typical situation, self-excited vortices are formed due to a nonvanishing curl of the plasma forces on the dust particles, e.g., in laboratory RF discharges, microgravity condition, and subsonic dusty plasma flow with low Reynolds numbers.[6,7] A nonvanishing or a nonzero component of the plasma force field's curl results in the dust particles' rotational motion, leading to the formation of vortices. Convection-induced vortex formation has also been reported that appears due to the presence of a temperature gradient along the top and bottom electrodes of a capacitively coupled RF plasma chamber.[8] In microgravity conditions, Fortov *et al.* studied the dynamics of dust particles where they showed that in the presence of a considerable ion drag force, a slight variation of the charge on the particles is sufficient for the formation of their vortex motion.[9] Dust particle vortex flow is also driven by a torque resulting from the nonconservative nature of ion drag force exerted on a dust particle.[10] Experiments have even been attempted to generate vortices by externally induced flow in dusty plasma, e.g., laser radiation, neutral gas flow, and probe induced flow.[11–16] Mitic *et al.* investigated the convective motion of dust particles in the presence of external controllable heating. They showed that, under such conditions, vortices in complex plasmas occur due to the neutral gas convection, with clouds of microparticles resembling convective clouds in the atmosphere. The mechanism responsible for the gas convection is the thermal creep along the inhomogeneously heated walls of the chamber.[17] In particular, vortex patterns are well known in hydrodynamics and other physical systems (e.g., aerodynamics) when fluids or gases flow past an obstacle or vice versa.

Morfill *et al.* observed a stable laminar shear flow (velocity ∼0.8 cm s⁻¹) around a spontaneously generated lentil shaped void.[18] A wake region is formed behind the obstacle separated from the laminar flow region by a mixing layer, which exhibited an instability growing on a scale much smaller than the hydrodynamic scale. Stable vortex flows are observed in the wake region. Jaiswal *et al.* investigated dynamical structures' formation by inducing dust flow toward a spherical obstacle over a range of flow velocities and obstacle biases.[19] Interestingly, nonlinear structures like bow shock and precursor solitons are observed when dusty plasma with supersonic speeds flows past obstacles.[20,21] There are also works on numerical simulation, where the interaction of both subsonic and supersonic dusty plasma flow with a square obstacle is studied.[22,23] In the subsonic and supersonic velocity range, von Karman vortex strait and bow shock were observed. The evolution of inertial waves emerging from an unsteady vortex source for strongly correlated dusty plasma has also been investigated using Molecular Dynamics (MD) simulation.[24] Dust vortices are also studied in magnetized dusty plasmas, both experimentally and in numerical simulations.[25,26] Dusty plasma fluid passing through a stationary dusty plasma forms dynamic dust structures (e.g., solitons and shocks) with a stable distribution of densities.[27] Normal dispersion of the medium and/or dissipation due to dust-neutral collisions compensate the non-linearity for forming such structures. A nonvanishing curl of the fluid flow velocity and inherent dissipative forces due to viscosity and neutral drag tends to organize the vortex's formation. An obstacle to the fluid flow path enforces the curl of the flow velocity. However, structure formation behind the obstacle varies with energy of the flow, geometry of the obstacle, and physical properties of the fluid.

We investigate here the pattern formation due to an externally generated dusty plasma flow past an obstacle. The obstacle is a circular dust void created by thin wire due to its sheath electric field. The sheath field decreases exponentially from the wire to the void boundary. The inward ion drag force and outward sheath electric force on the dust particles balance at the void boundary. The experiment is novel and clearly demonstrates the vortex pair formation in the wake behind the void at a particular range of velocities. A Molecular Dynamics (MD) simulation is carried out, and results are compared with the experimental observation.

II. EXPERIMENTAL SETUP

The experiment is done in a simple borosilicate glass cylinder of 100 cm in length and 15 cm in radius.[28] A schematic of the device is shown in Fig. 1. The base pressure on the order of ∼10⁻⁵ mbar is created while the working pressure is maintained at $(1-3) \times 10^{-2}$ mbar by injecting pure argon gas. The plasma is produced by applying RF power (5 W, 13.56 MHz) through a matching network (MN) to a thin aluminum strip placed on the chamber's outer surface. Dust grains are gold coated monodisperse silica particles with diameter 5 ± 0.1 μm and mass density 2.6 g cm⁻³. The plate P2 is mechanically lifted up to generate the dust flow toward the plate (P1). Details of the dusty plasma and flow generation technique may be found elsewhere.[27] In a single shot, the flow sustains for a 1000 ms–2000 ms (depending on flow speed) above P1, and video recording is done for entire duration and length (∼20 cm). After completion of each lift/flow, the dust particles are taken back to the plate P2 by lowering the level of P2 with respect to P1, leaving behind the stationary dusty plasma fluid over P1. Dust density in both sections (above P1 and P2) is stabilized within
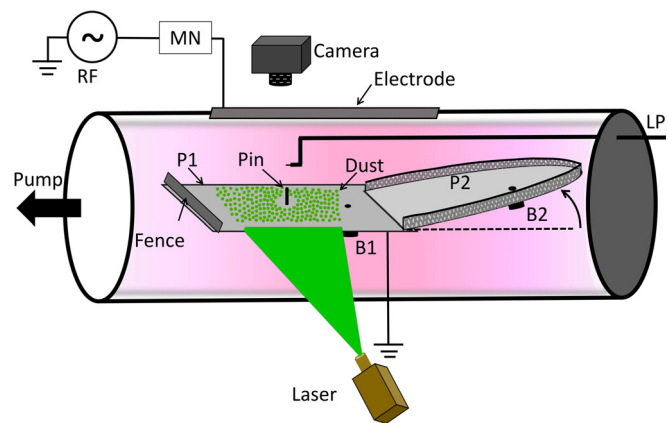

FIG. 1. Schematic diagram of the experimental setup. P1—graphite plate, P2—steel plate, B1, B2—buzzers, LP—Langmuir probe, RF—radio frequency power supply, MN—matching network.

few seconds and made ready for next flow shot. It is important to note that the flow generation method neither affects the plasma parameters nor the discharge condition. Therefore, dusty plasma parameters (charge, temperature, etc.) remain unaltered all throughout the experiment. The plasma is characterized by a radio frequency (RF) compensated cylindrical Langmuir probe. Measured ion density is $n_i = 2 \times 10^8$ cm⁻³ and electron temperature $T_e \sim 5$ eV. The plasma potential is measured with respect to the ground (30 cm × 14.5 cm graphite plate and the side flanges). The measured value of the plasma potential is +38 V. The average charge Q_d on a dust particle is calculated from the force balance between the upward sheath electrostatic force above the plate ($Q_d E_h$, where E_h is the electric field at levitation height h) and downward gravitational force ($m_d g$, where $m_d = 1.7 \times 10^{-13}$ kg is the dust mass and g is the acceleration due to gravity). Details of the measurement of sheath electric field at the levitation height have been described elsewhere.[28] At a typical dust levitation height of (0.7–1.0) cm, the measured sheath electric field E_h is found to be (4–6) V cm⁻¹. The dust charge is then calculated using the relation $Q_d = m_d g / E_h$ and is found to be [∼(1.7–2.6) × 10⁴ e] for the present experimental condition. The Q_d value obtained as such closely agrees with the dust charge calculated by using the Orbital Motion Limited (OML) theory. In an another experiment, under similar experimental conditions, Nakamura and Ishihara also measured the average dust charge on a 5 μm diameter particle on the order of ∼10⁴ e.[29] Dust particles and plasma ions are considered to be at much lower temperature than that of the electrons (T_d/T_e, $T_i/T_e \sim 0.1$). The dust density n_d in the stationary dusty plasma is $(8 \times 10^2 - 1.43 \times 10^3)$ cm⁻³ (interparticle distance "a" ∼ 0.6 0 ± 0.05 mm). In the presence of dust flow, the interparticle distance reduces to (0.30 ± 0.05) mm and corresponding $n_d = (5.57 \times 10^3 - 1.52 \times 10^4)$ cm⁻³. The Coulomb coupling parameter is calculated using the relation $\Gamma = (Z_d^2 e^2 / 4\pi\epsilon_0 a k_B T_d) \exp(-a/\lambda_D)$, where Z_d is the dust charge number, e is the electronic charge, ϵ_0 is the absolute permittivity, k_B is the Boltzmann constant, T_d is the dust temperature, and λ_D is the linearized Debye length, i.e., the ion Debye length. For $Z_d = 2 \times 10^4$, $a = 0.6$ mm, $\lambda_D = 0.3$ mm, and dust temperature T_d (∼$T_i \sim 0.1$ T_e)V, Γ is found to be ∼260. The dusty plasma medium remains at strongly

coupled state. For $\kappa = 2$, the critical Γ above which dust crystallization occurs is ~ 400.

   A tungsten wire (0.1 mm in diameter, 1.5 cm long) is placed vertically on the plate P1. The surface potential of the pin is -32 V with respect to the plasma potential, and it creates a circular void (1.7 cm in diameter) with sharp boundary due to balance of outward electrostatic force and inward ion drag force.[30] Dust flow (from P2) through the stationary dusty plasma (on plate P1) is created with flow velocity range 3–10 cm s^{-1}. A higher velocity flow from P2 is associated with a shock or soliton like wave front.[27] The linear dust acoustic wave speed is measured to be 4.5 cm s^{-1}. A dust acoustic wave is excited by applying a small amplitude sinusoidal pulse into the grid fence.[27] The theoretical calculations using the formula for dust acoustic velocity, $C_{DAW} = \sqrt{(k_B T_i Z_d^2 n_d / m_d n_i)}$ (k_B is the Boltzmann constant and T_i is the ion temperature), yield $C_{DAW} = 3.4$ mm s^{-1}, with the given parameters and $T_i = 0.03$ eV. However, experimentally measured C_{DAW} is nearly 10 times larger, probably due to the ion temperature T_i in such devices is rather large $(T_e/T_i) \sim 10$. On the other hand, the dust charge number Z_d also contributes to the C_{DAW}. In our case, considering $T_i \sim 0.1\ T_e$ (~ 0.5 eV) and $Z_d \sim 2 \times 10^4$, C_{DAW} reaches to a value of ~ 3.06 cm s^{-1} which is close to the experimentally measured value. Particles are illuminated by the laser light scattering technique using a green laser sheet (532 nm, 30 mW). Dust dynamics are recorded using a high resolution video camera [at both 30 frames per second (fps) and 100 fps].

III. RESULTS AND DISCUSSIONS
A. Experimental analysis

   Snapshots converted from videos recorded at 30 fps are shown in Fig. 2. They represent the examples of pattern formation behind the dust void for different dust flow velocities. The dust fluid velocity v_d in the medium is maintained in the range of 3–10 cm s^{-1} by controlling the lift (of P2). The top image in Fig. 2(a) represents a flow with $v_d \sim 3$ cm s^{-1}, and the snapshot is at time t = 1370 ms from a reference time (t = 0 when dust flow reaches the right edge of the images).

   The flow breaks into two parts when encounters the potential barrier at the void boundary and reunite again behind the void. Vortices are not formed fully for such flow with slower velocity. Figure 2(b) represents an image with dust fluid flow velocity $v_d \sim 4.5$ cm s^{-1} at t = 1033 ms, showing the vortex pair formation behind the void. The void boundary in the upstream is more compressed (due to higher dust pressure). The boundary is elongated behind the void, and a pair of vortex is formed in the wake with two clear eyes (shown by the arrow marks). It is observed that the vortex pair formation occurs within a very narrow range of critical velocity ~ 4.0–7.0 cm s^{-1}. Vortices are not formed for larger flow velocity $v_d \sim 8$ cm s^{-1} [Fig. 2(c)]. Flow trajectories behind the void are elongated, and dynamics at the intersection is rather complex due to cross flow at high speed. It is noted that dust flow with unsteady laminar velocity with optimum dust density is required to generate the vortex when flow past the void. This is achieved by combining the stationary dust on plate P1 pushed by the flowing dust of nearly equal density from P2. In the absence of stationary dust, the flow from P2 results in the confluence of the bifurcated flows with some trapped particles behind the void without forming any vortex structure.
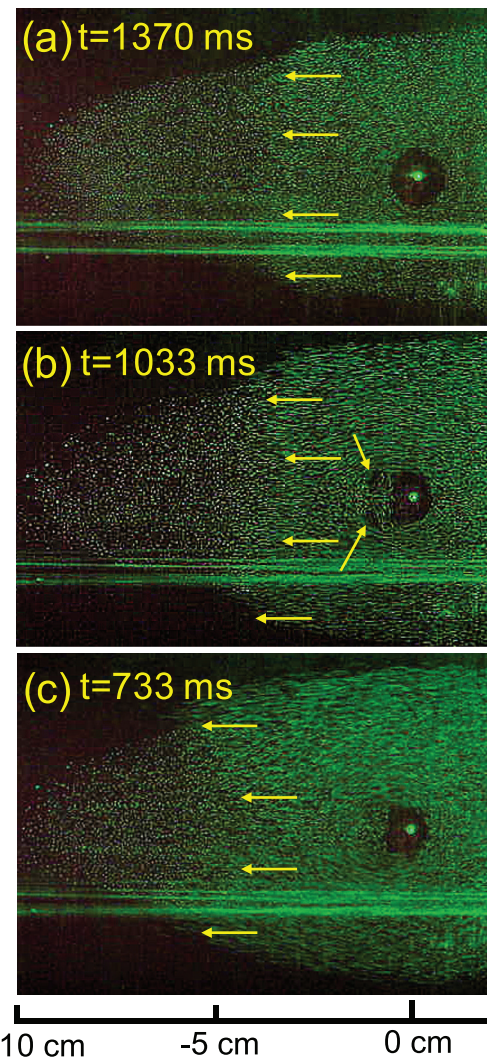

FIG. 2. Typical snapshots showing structures formed behind the void with different v_d. (a) 3 cm s^{-1}, (b) 4.5 cm s^{-1}, and (c) 8 cm s^{-1}. The parallel arrows show the direction and location of the dust front. Two arrows behind the void (b) show the formation of vortex pair.

   Typical image sequences of temporal development of the vortex pair are shown in Fig. 3 (Multimedia view) when $v_d \sim 5$ cm s^{-1}.

   At the beginning of the vortex formation, the curved flow lines close to the void boundary interact with the stationary layer and starts to swirl on each side (dotted arrow marks). The swirling occurs for the particles flowing close to the boundary since they are bound to travel through the void's curved boundary. This generates the curl in the flow. However, the outer part of the flow lines flows past without swirling. With time, the first group of particles flowing close to the void boundary completes the circulation to grow into a vortex pair. The fully grown vortices are seen at t = 1033 ms (b), with more dust particles swirling around the eyes. As the flow continues maintaining constant particle flux, the vortex structures sustain till (c) t = 1167 ms and remains faintly visible until t = 1233 ms. The time for the vortex
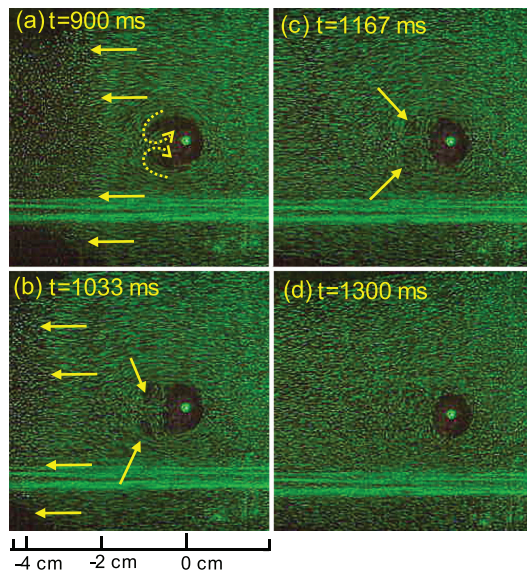
FIG. 3. Sequence of snapshots showing vortex pair formation behind the void. $v_d \sim 4.5$ cm s^{-1}. The parallel arrows show the direction of the dust flow. Dotted curved traces with arrows in (a) indicate initial flow trajectories. The arrows in (b) and (c) show the vortices. Vortex vanishes with time when flow is nearly over (d). The pin position at x $\sim$ 0 cm. An example of video (recorded at 30 fps) showing the vortex generation can be seen online. Multimedia view: https://doi.org/10.1063/5.0022356.1

growth is $\sim$200 ms (from the time the particles meet behind the void) and survives for 300–400 ms (depending on the duration of flow). In the case of Morfill et al., it is observed that the stable vortex flows are generated in the wake region due to momentum transfer between the two fluid regimes.[18] Whereas in the present experiment, the curl of the dust flow itself flowing toward the low density region generates the vortex pair behind the void. The rotational frequency of the vortex is estimated $\sim$3 Hz. As soon as the flow expires in the upstream, the vortex structures disappear as seen in (d). In the absence of flow, the force balance at the void boundary is due to outward sheath electric field and inward ion drag which is equal to $\sim 1 \times 10^{-13}$ N. The value of the ion drag force is calculated from the Barnes model, usually expressed as a sum of the collection and the orbital forces, $F_i = F_{coll} + F_{orb}$.[31,32] The collection force F_{coll} is associated with the momentum transfer from the ions that are collected by the dust particle, and the orbital force F_{orb} occurs due to the momentum transfer from the ions that are elastically scattered in the electric field of the charged particle. For the calculation of the ion drag force, the linearized Debye length, i.e., the ion Debye length, is used. The detail calculation of the force balance mechanism at the void boundary may be found elsewhere.[30] The dust flow bifurcates at the upstream boundary of the void due to its repulsive electrostatic force, and the curl of the flow velocity develops along the boundary region of the void. The Mach velocity of the flow for the vortex formation is close to unity. Interestingly few dust particles are off tracked from the circulation and undergo a reverse flow along the void boundary up to half of the void circle. However, we do not have a proper explanation for these phenomena presently. It will be investigated in future.

The Reynolds number Re $= \rho v_d L / \eta$ is calculated for the dust flow velocity $\sim$ (3–10) cm s^{-1}. Here ρ is the mass density and η is the shear viscosity of the fluid. The characteristic length $L = 1.7$ cm (void diameter). $\eta = \sqrt{3} \hat{\eta} m_d n_d \omega_E a^2$ is calculated using experimental parameters ($m_d \sim 1.7 \times 10^{-13}$ kg, $n_d \sim 9 \times 10^9$ m^{-3}, $\omega_E = \left(\omega_{pd} / \sqrt{3} \right)$ the Einstein frequency, and $\omega_{pd} \sim 247.5$ s^{-1}). The parameters are presented in Table I. The normalized shear viscosity $\hat{\eta}$ of the dusty plasma fluid is a function of the Coulomb coupling parameter Γ.[33,34] The shear viscosity η for the present experimental condition is estimated as $\sim 9 \times 10^{-9}$ Pascal-second (Pa s) and the corresponding kinematic viscosity $\nu(= \eta/\rho)$ is $\sim$0.088 cm^2 s^{-1}. The estimated values of ν and η are within the range of earlier reported values for dusty plasma fluid[35–38] ($\nu \sim 0.01$–0.1 cm^2 s^{-1} and $\eta \sim 10^{-11}$–10^{-9} Pa s). The Reynolds numbers for the present experiment are estimated to be Re $\sim$50–190 for the flow velocity range $v_d \sim$ (3–10) cm s^{-1}, and the vortex pair form behind the void when Reynolds number falls in the range $\sim$60–90.

The flow is analyzed using a MATLAB based open access Particle Image Velocimetry (PIV) code to study the evolution of the vortex pair and its vorticity.[39] PIV analysis is performed on the consecutive still images of a 100 fps video ($v_d \sim 4.5$ cm s^{-1}) flowing from 0 s to 1.0 s. A total of 100 still images of pixel resolution 357×357 sq. pixel (3×3 cm^2) in an interval of 10 ms are fed into the software. An interrogation window size of 32×32 sq. pixel and spacing of 16×16 sq. pixel are chosen to construct the velocity vector fields. Figure 4 shows the velocity vector fields (v $= \sqrt{(v_x^2 + v_y^2)}$), and the color mapping is the magnitude of the vorticities represented by the color bar in s^{-1}. Each image in Fig. 4 is an average of 10 consecutive image frames. The position of void (dotted red circle) and the pin (point) at the center of the void is drawn in Fig. 4(a), which is similar for all the other subfigures. In the PIV images, the size of the void seems to be smaller than the actual size (1.7 cm) since these are at instances when the dust flow reaches near the void. As the dust void is not a rigid obstacle, its size gets deteriorated and becomes smaller when the flow approaches.

It is mentioned before that flow gets slowed down in front of the void due to the repulsive sheath electric field force and follows a curved path close to the boundary on both sides of the void. The slowing down of the particles in front of the void is clearly seen by comparing the velocity vectors' length in Figs. 4(a) and 4(b). The backflow of the incoming dust particles (due to repulsive sheath electric field force of the pin) is also observed in Fig. 4(b). The bifurcated flows meet again in the wake region behind the void in Fig. 4(c). The vortex pair's generation is evident from the curl of the vectors from Figs. 4(d)–4(f). The vorticity ($\nabla \times \vec{v}_d$) of the fully formed vortex pair is about $\sim$20–25 s^{-1} (which is nearly twice the measured corresponding

TABLE I. Plasma parameters involved in calculating the shear viscosity η.

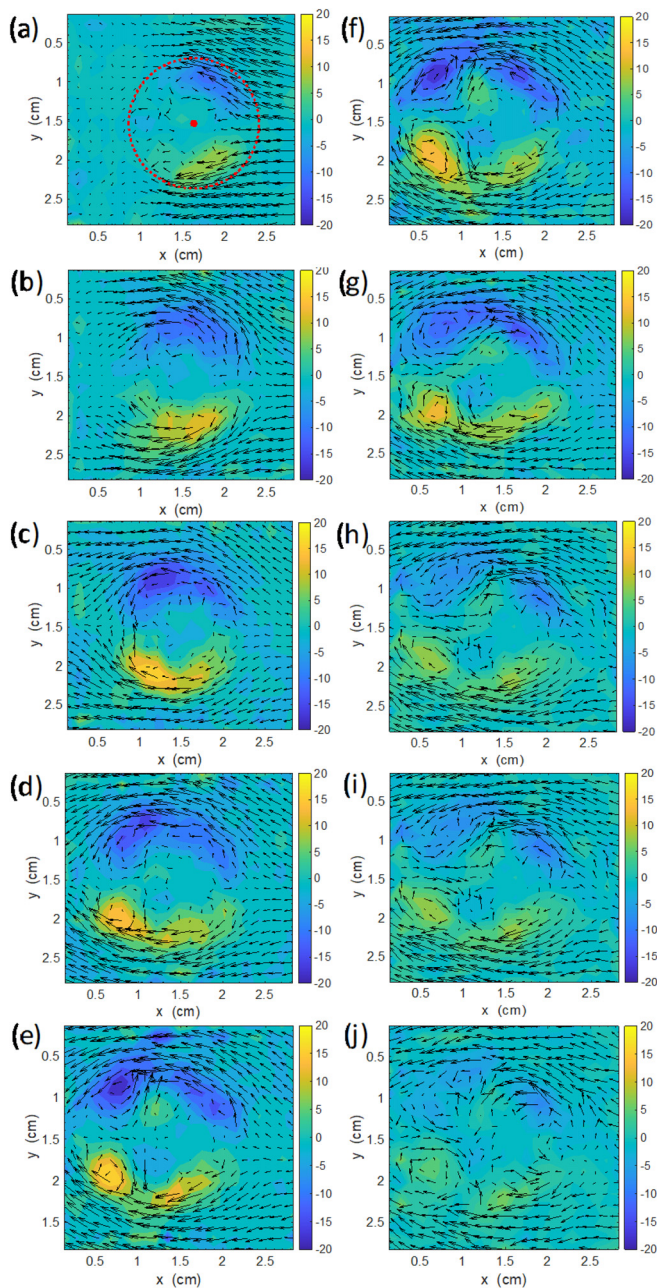| Plasma parameters	Value
Dust mass, m_d	1.7×10^{-13} kg
Dust density, n_d	9×10^9 m^{-3}
Einstein frequency, ω_E	142.89 s^{-1}
Interparticle distance, a	3×10^{-4} m

FIG. 4. PIV analysis showing the time evolution of the vortices for a duration of 1.00 s. The vorticity profile and velocity vectors drawn from (a) (0.53–0.62)s, (b) (0.63–0.72)s, (c) (0.73–0.82)s, (d) (0.83–0.92)s, (e) (0.93–1.02)s, (f) (1.03–1.12)s, (g) (1.13–1.22)s, (h) (1.23–1.32)s, (i) (1.33–1.42)s, (j) (1.43–1.52)s are shown. The color bar shows the value of vorticity in s^{-1}. The dotted circle in (a) shows the original position of the void boundary before the flow and the dot at the center of the circle represents the pin's position. The coordinates (x, y) = (1.6 cm, 1.5 cm) correspond the pin position.

angular frequency), and they survive for about ~0.4 s. As the incoming flow gradually diminishes, the vortex structure deforms and breaks up into smaller vortices, which is observed in Figs. 4(g)–4(i). During the deformation phase, the vorticity decreases to 15 s^{-1} in Fig. 4(g)

and then to 10 s^{-1} in Fig. 4(i). The vortices finally tend to weaken, which is seen in Fig. 4(j) and then disappear. The velocity vectors of all the 100 image frames are together plotted in Fig. 6(a) showing the vortex pair's clear formation, and the averaging of the instantaneous vorticities reduces the final vorticity to ~10 s^{-1}. In other dusty plasma experiments of vortex formation, the estimated vorticities of spontaneous and induced vortices are around ~(5–10) s^{-1}. Mulsow *et al.* observed spontaneous vortex motions in dust clusters, the average vorticity of which is estimated as ~8 s^{-1}. Ticos *et al.* also studied the interaction of a high energetic electron beam with a dust crystal due to which a laminar dust flow is generated in the path of the beam. The vorticity of the perturbed flow reaches to about ±5–10 s^{-1}. [40,41]

B. Simulation

A molecular dynamics simulation is carried out to investigate the formation of a counter-rotating vortex pair behind a dust void using an open-source classical MD code LAMMPS.[42] For the simulation study, a three-dimensional (3D) cubic box with point dust particles has been created. The dust particles interact with each other via Yukawa form of the electrostatic interaction potential. 360 000 grains (with periodic boundary conditions) are created in the simulation box with $L_x = 304.65a$ (0 to 304.65a), $L_y = 609.3a$ (0 to 609.3a), and $L_z = 8.12a$ (0 to 8.12a) along X, Y, and Z directions, respectively, where $a = (3/4\pi n_d)^{1/3}$ is the Wigner–Seitz radius in three-dimension and n_d corresponds to dust density of the medium. In the center of the 3D system, a cylindrical obstacle with axis along Z-axis has been created. The coordinate of cylinder axis in the X and Y dimensions is 152.32a and 304.65a, respectively. To keep in mind the cylinder's sheath electric field, an exponentially decaying repulsive force from the cylinder has been applied on the dust micro-particles, mathematically $F_{sh} = F_0 \exp(-r/\lambda_C)$. Here r is the distance from the cylinder center to the particle position, and λ_C is the Debye length for the repulsive force from the cylinder. We have taken $\lambda_C = 6 \times 10^{-3}$ m and $F_0 = 1 \times 10^{-13}$ N. The value of λ_C is optimized to create a void of experimental size in the medium (~1.7 cm). In the simulation, we have taken the dust grain mass $m_d = 1.7 \times 10^{-13}$ kg, charge $Q_d = -20\,000e$ (e is an electronic charge), and $a = 2.9542 \times 10^{-4}$ m. The "a" used in simulation is very close to the experimental $a = 3 \times 10^{-4}$ m. The screening parameter κ is chosen to be 1.4771 which sets the plasma Debye length in the simulation as $\lambda_D = 2.0 \times 10^{-4}$ m. We have chosen simulation time step as 0.0001 s so that phenomena occurring at dust response time scale can be easily resolved. Thermodynamical equilibrium state for a given coupling parameter Γ is achieved by generating positions and velocities from canonical ensemble using the Nose–Hoover thermostat.[43,44] After about a canonical run for 40 000 time step, we disconnected the canonical thermostat and ran a simulation for about 20 000 time step micro-canonically to test the energy conservation. After the micro-canonical run, the dust medium achieves thermodynamical equilibrium with the desired value of Γ.

To create the experimental scenario, we have divided simulation box into two layers with lower one having dimension $L_x = 0$ to 304.65a, $L_y = 0$ to 609.3a, and $L_z = 0$ to 4.062a and another upper one with dimension $L_x = 0$ to 304.65a, $L_y = 0$ to 609.3a, and $L_z = 4.062a$ to 8.124a. A sketch of the configuration is shown in Fig. 5(a). The lower layer and the upper layer are shown in filled blue and shaded green color, respectively. We have set the lower layer static with
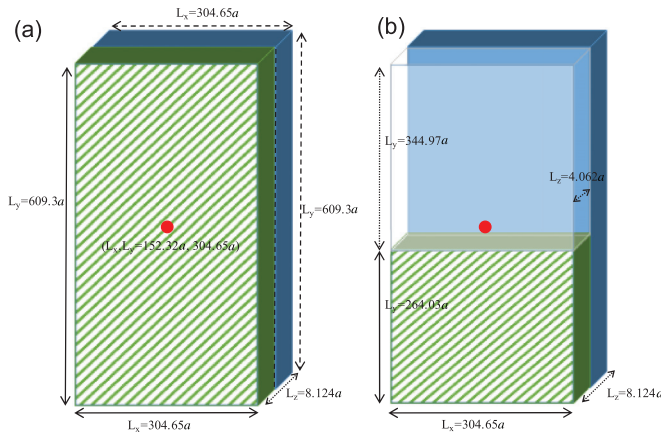
FIG. 5. (a) The simulation box with two layers of dust particles. The dimension of the lower layer (blue filled box) is $L_x = 0$ to $304.65a$, $L_y = 0$ to $609.3a$, and $L_z = 0$ to $4.062a$ and the upper layer (green shaded box) is $L_x = 0$ to $304.65a$, $L_y = 0$ to $609.3a$, and $L_z = 4.062a$ to $8.124a$. (b) The configuration of the simulation box just before the flow is initiated. In the upper layer, a region $L_x = 0$ to $304.65a$, $L_y = 264.03a$ to $609.3a$, and $L_z = 4.062a$ to $8.124a$ is deleted. The red filled circle in both (a) and (b) represents the position of the cylinder (L_x, $L_y = 152.32a$, $304.65a$).

average flow velocity 0 and in the upper layer deleted a region $L_x = 0$ to $304.65a$, $L_y = 264.03a$ to $609.3a$, and $L_z = 4.062a$ to $8.124a$, as shown in Fig. 5(b). The deleted part of the upper layer is represented as transparent, and the remaining upper layer is kept in shaded green respectively. The red filled circle in Figs. 5(a) and 5(b) represents the position of the cylinder (L_x, $L_y = 152.32a$, $304.65a$). We have applied a constant force $F_{flow} = 2.5 \times 10^{-14}$ N along Y direction on all particles of the remaining upper layer $L_x = 0$ to $304.65a$, $L_y = 0$ to $264.03a$, and $L_z = 4.062a$ to $8.124a$ for the time span from $t = 0$ to $t = 0.8$ s to create flow of the particles.

The motion of the i-th particle with mass m_d is governed by the following equation:

$$m_d \ddot{\vec{r}}_i = \sum_j \nabla U_{ij} + F_{sh} + F_{flow} + F_r + F_f,$$

where $\vec{F}_f = -m_d \nu \vec{v}$ is the neutral drag force due to the relative velocity $\vec{v}$ between the dust particles and neutral particles and force $F_r = \sqrt{(k_B T_n m_d \nu)/dt}$ is random kicks suffered by dust grains by collisions with neutral atoms.[42,45] Where dt and T_n are the time step of simulation and background neutral gas temperature, respectively. Here, ν is the damping coefficient which chosen to be 0.5 s^{-1} in the simulation. The average flow velocity is 5.5 cm s^{-1}, and flow reaches the obstacle at 0.11 s. When the flowing particles approach the void, they are repelled by the sheath electrostatic force F_{sh} which results in the flow to break into two symmetric parts and meet again behind the void. When the flow velocity reaches close to the experimental value, the vorticity creates circulation in each broken symmetric part leading to the formation of a vortex pair (the vortices rotate in the opposite direction to each other). The value of the vorticity is estimated to be ~ 8 s^{-1}, which is close to the average vorticity estimated in the experiment, i.e., ~ 10 s^{-1}. A typical snapshot of velocity quiver plot after the formation of the vortex pair at 2.21 s in the simulation is shown in Fig.
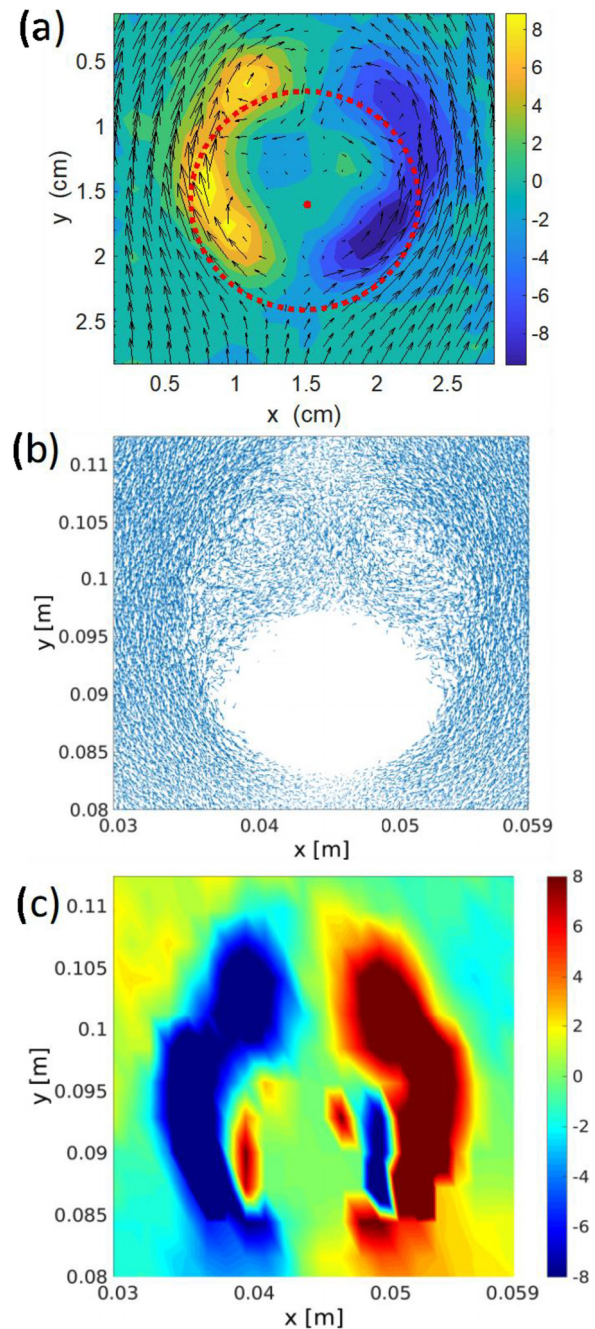

FIG. 6. (a) PIV quiver plot of 100 consecutive image frames with an interval of 10 ms drawn from experimental data. The dotted circle in (a) shows the original position of the void boundary before the flow and the dot at the center of the circle represents the pin's position. The coordinates (x, y) = (1.5 cm, 1.6 cm) correspond to the pin position. For better comprehension, a resemblance in flow direction with simulation is made by orienting the experimental data 90° clockwise. The vectors show the particles' flow direction, and the color bar shows the value of vorticity in s^{-1}. (b) and (c) show the simulation results. (b) A typical snapshot of velocity quiver plot after the formation of the vortex pair at 2.21 s. (c) The $\hat{z}$ component of the vorticity ($\Omega = \nabla \times \vec{v}_d$) of the medium. The color bar shows the value of vorticity in s^{-1}.

6(b). The $\hat{z}$ component of the vorticity ($\Omega = \nabla \times \vec{v_d}$) of the medium is plotted in Fig. 6(c). The vorticity map clearly shows the formation of two oppositely rotating vortices behind the obstacle. The color bar represents the vorticity of the medium in unit of s^{-1}. It is observed that the experimental and simulation results complement each other. The vortex pair for a specific range of velocities has been observed in simulation also. In the simulation, vortices are only forming in the velocity interval 4–15 cm s^{-1}. This difference in the flow velocity range with that of the experiment may be due to the play in the plasma parameters involved.

IV. CONCLUSION

In summary, we demonstrate the clear evolution of a pair of counter-rotating symmetric vortices when dusty plasma flows past an obstacle/void associated with electrostatic potential. The dust density and the velocity of the flowing dust are delicately maintained in the experiment. The Reynolds number for vortex formation in the present experiment is in the range $60 \leq Re \leq 90$. In hydrodynamic fluid, the corresponding Re range is $5 \leq Re \leq 40$, which is much lower. This larger range in the case of dusty plasma fluid arises due to a larger ρ/η ratio (i.e., kinematic viscosity) than that in hydrodynamic fluid. In the present experiment, vortex shedding is not observed, possibly due to the limitation of continuous dusty plasma fluid flow for longer time as well as due to larger neutral drag, which introduces heavy dissipation. A detailed investigation on the breaking of vortices into smaller vortices will provide more insight into the observed phenomena. The molecular dynamics simulation replicates the PIV analysis of observed phenomena. Our study as a whole opens up a comprehension of flow past an obstacle in a strongly coupled dusty plasma fluid, and the results may be of interest in the interpretation of structures observed in space plasmas.

DATA AVAILABILITY

The data that support the findings of this study are available within the article.

REFERENCES

[1]G. E. Morfill and A. V. Ivlev, Rev. Mod. Phys. **81**, 1353 (2009).
[2]J. H. Chu and I. Lin, Phys. Rev. Lett. **72**, 4009 (1994).
[3]H. Thomas, G. E. Morfill, V. Demmel, J. Goree, B. Feuerbacher, and D. Möhlmann, Phys. Rev. Lett. **73**, 652 (1994).
[4]H. M. Thomas and G. E. Morfill, Nature **379**, 806 (1996).
[5]P. Bliokh, V. Sinistin, and V. Yaroshenko, *Dusty and Space Gravitational Plasmas in Space* (Kluwer Academic Publishers, Dordrecht, 1995).
[6]M. Schwabe, S. Zhdanov, C. Räth, D. B. Graves, H. M. Thomas, and G. E. Morfill, Phys. Rev. Lett. **112**, 115002 (2014).
[7]J. K. Meyer, J. R. Heinrich, S. H. Kim, and R. L. Merlino, J. Plasma Phys. **79**, 677 (2013).
[8]S. Shimizu, B. Klumov, T. Shimizu, H. Rothermel, O. Havnes, H. M. Thomas, and G. E. Morfill, J. Geophys. Res. **115**, D18205, https://doi.org/10.1029/2009JD013375 (2010).
[9]V. E. Fortov, O. S. Vaulina, O. F. Petrov, V. I. Molotkov, A. V. Chernyshev, A. M. Lipaev, G. Morfill, H. Thomas, H. Rotermell, S. A. Khrapak *et al.*, J. Exp. Theor. Phys. **96**, 704 (2003).
[10]K. B. Chai and P. M. Bellan, Phys. Plasmas **23**, 023701 (2016).
[11]M. Schwabe, M. Rubin-Zuzic, S. Zhdanov, A. V. Ivlev, H. M. Thomas, and G. E. Morfill, Phys. Rev. Lett. **102**, 255005 (2009).
[12]M. Klindworth, A. Melzer, A. Piel, and V. A. Schweigert, Phys. Rev. B **61**, 8404 (2000); T. Miksch and A. Melzer, Phys. Rev. E **75**, 016404 (2007).
[13]D. A. Law, W. H. Steel, B. M. Annaratone, and J. E. Allen, Phys. Rev. Lett. **80**, 4189 (1998); G. Uchida, S. Iizuka, T. Kamimura, and N. Sato, Phys. Plasmas **16**, 053707 (2009).
[14]V. I. Vladimirov, L. V. Deputatova, A. P. Nefedov, V. E. Fortov, V. A. Rykov, and A. V. Khudyakov, J. Exp. Theor. Phys. **93**, 313 (2001).
[15]M. Schwabe, L. J. Hou, S. Zhdanov, A. V. Ivlev, H. M. Thomas, and G. E. Morfill, New J. Phys. **13**, 083034 (2011).
[16]M. A. Fink, S. K. Zhdanov, M. Schwabe, M. H. Thoma, H. Höfner, H. M. Thomas, and G. E. Morfill, Europhys. Lett. **102**, 45001 (2013).
[17]S. Mitic, R. Sutterlin, A. V. Ivlev, H. Hofner, M. H. Thoma, S. Zhdanov, and G. E. Morfill, Phys. Rev. Lett. **101**, 235001 (2008).
[18]G. E. Morfill, M. Rubin-Zuzic, H. Rothermel, A. V. Ivlev, B. A. Klumov, H. M. Thomas, and U. Konopka, Phys. Rev. Lett. **92**, 175004 (2004).
[19]S. Jaiswal, M. Schwabe, A. Sen, and P. Bandyopadhyay, Phys. Plasmas **25**, 093703 (2018).
[20]Y. Saitou, Y. Nakamura, T. Kamimura, and O. Ishihara, Phys. Rev. Lett. **108**, 065004 (2012).
[21]S. Jaiswal, P. Bandyopadhyay, and A. Sen, Phys. Rev. E **93**, 041201(R) (2016).
[22]H. Charan and R. Ganesh, Phys. Plasmas **23**, 123703 (2016).
[23]H. Charan and R. Ganesh, Phys. Plasmas **25**, 043706 (2018).
[24]A. Gupta and R. Ganesh, Phys. Plasmas **27**, 050701 (2020).
[25]M. Choudhary, R. Bergert, S. Mitic, and M. H. Thoma, Phys. Plasmas **27**, 063701 (2020).
[26]P. Kumar and D. Sharma, Phys. Plasmas **27**, 063703 (2020).
[27]S. K. Sharma, A. Boruah, and H. Bailung, Phys. Rev. E **89**, 013110 (2014); A. Boruah, S. K. Sharma, H. Bailung, and Y. Nakamura, Phys. Plasmas **22**, 093706 (2015); S. K. Sharma, A. Boruah, Y. Nakamura, and H. Bailung, *ibid.* **23**, 053702 (2016).
[28]S. K. Sharma, R. Kalita, Y. Nakamura, and H. Bailung, Plasma Sources Sci. Technol. **21**, 045002 (2012).
[29]Y. Nakamura and O. Ishihara, Phys. Plasmas **16**, 043704 (2009).
[30]Y. Bailung, T. Deka, A. Boruah, S. K. Sharma, A. R. Pal, J. Chutia, and H. Bailung, Phys. Plasmas **25**, 053705 (2018).
[31]A. Melzer, *Introduction to Colloidal (Dusty) Plasmas*, Lecture Notes (Institute fur Physik, Ernst-Moritz-Arndt-Universitat, Greifswald, 2005).
[32]M. S. Barnes, J. H. Keller, J. C. Forster, J. A. O'Neill, and D. K. Coultas, Phys. Rev. Lett. **68**, 313 (1992).
[33]T. Saigo and S. Hamaguchi, Phys. Plasmas **9**, 1210 (2002).
[34]Z. Donko, J. Goree, P. Hartmann, and K. Kutasi, Phys. Rev. Lett. **96**, 145003 (2006).
[35]V. Nosenko and J. Goree, Phys. Rev. Lett. **93**, 155004 (2004).
[36]R. Heidemann, S. Zhdanov, K. R. Sutterlin, H. M. Thomas, and G. E. Morfill, Eur. Phys. Lett. **96**, 15001 (2011).
[37]A. Gavrikov, I. Shakova, A. Ivanov, O. Petrov, N. Vorona, and V. Fortov, Phys. Lett. A **336**, 378 (2005).
[38]E. W. Hones, J. Birn, S. J. Bame, J. R. Asbridge, G. Paschmann, N. Sckopke, and G. Haerendel, J. Geophys. Res. **86**, 814, https://doi.org/10.1029/JA086iA02p00814 (1981).
[39]Z. J. Taylor, R. Gurka, G. A. Kopp, and A. Liberzon, IEEE Trans. Instrum. Meas. **59**, 3262 (2010).
[40]M. Mulsow, M. Himpel, and A. Melzer, Phys. Plasmas **24**, 123704 (2017).
[41]C. M. Ticos, D. Ticos, and J. D. Williams, Phys. Plasmas **26**, 043702 (2019).
[42]S. Kumar and A. Das, Phys. Rev. E **97**, 063202 (2018).
[43]S. Nos, Mol. Phys. **52**, 255 (1984).
[44]W. G. Hoover, Phys. Rev. A **31**, 1695 (1985).
[45]S. Plimpton, J. Comput. Phys. **117**, 1 (1995).